Atherosclerosis 310 (2020) 93–101

Contents lists available at ScienceDirect

Atherosclerosis

journal homepage: www.elsevier.com/locate/atherosclerosis

3D confocal microscope imaging of macromolecule uptake in the intact brachiocephalic artery

Marta Dazzi[1], Ethan M. Rowland[1], Zahra Mohri, Peter D. Weinberg*

Department of Bioengineering, Imperial College London, London, SW7 2AZ, UK

HIGHLIGHTS

- Homogenising the refractive index of arterial tissue increases confocal imaging depth.
- Tracer uptake can be imaged in intact curved or branched segments.
- We demonstrate and validate the method at the rat aorto-brachiocephalic junction.
- The detected pattern of permeability is consistent with patterns of lesions and flow.

ARTICLE INFO

Keywords:
BABB
Confocal microscopy
Permeability
Endothelium
Mass transport

ABSTRACT

Background and aims: Elevated uptake of plasma macromolecules by the arterial wall is an early event in atherogenesis. Existing optical techniques for detecting macromolecular tracers in the wall have poor depth penetration and hence require *en face* imaging of flattened arterial segments. Imaging uptake in undistorted curved and branched vessels would be useful in understanding disease development.
Methods: Depth penetration was increased by applying optical clearing techniques. The rat aorto-brachiocephalic junction was imaged intact by confocal microscopy after it had been exposed to circulating rhodamine-labelled albumin *in vivo*, fixed *in situ*, excised and then cleared with benzyl alcohol/benzyl benzoate. Tracer uptake was mapped onto a 3D surface mesh of the arterial geometry.
Results: Tracer fluorescence was detectable throughout the wall closest to the objective lens and, despite a vessel diameter of c. 1 mm, in the wall on the other side of the artery, across the lumen. By tile scanning, tracer concentrations were mapped in the aorta, the brachiocephalic artery and their junction without opening or flattening either vessel. Optical clearing was also shown to be compatible with immunofluorescent staining and imaging of experimental atherosclerosis.
Conclusions: The technique obviates the need for labour-intensive sample preparation associated with standard *en face* imaging. More importantly, it preserves arterial geometry, facilitating co-localisation of uptake maps with maps of biomechanical factors, which typically exist on 3D surface meshes. It will permit the correlation of haemodynamic wall shear stress with macromolecule permeability more accurately in regions of high curvature or branching, such as in the coronary arteries.

1. Introduction

Elevated net uptake of circulating macromolecules by the arterial wall is thought to be an early event in the atherosclerotic process. Measuring it could provide insight into disease development. Early studies used radiotracers but current techniques most often rely on fluorescent tracers, quantified in *post mortem* specimens. As technology has advanced, detection systems have moved from microscopes and photographic film, through widefield microscopes with intensified or cooled CCD cameras, to confocal microscopes with photomultiplier tubes [1–5]. In our own implementation of the latter, rhodamine-labelled albumin tracer is administered *in vivo* and left to circulate in the vasculature for periods of 10 min to 3 h. The animal is then sacrificed, the vessels are perfused with fixative and the arteries are excised and imaged with a laser scanning confocal microscope [1]. Because depth penetration is poor (< 100 μm [6]) and the inner layers of the wall are

* Corresponding author.
E-mail address: p.weinberg@imperial.ac.uk (P.D. Weinberg).
[1] These authors contributed equally to this work.

https://doi.org/10.1016/j.atherosclerosis.2020.07.002
Received 21 January 2020; Received in revised form 20 June 2020; Accepted 2 July 2020
Available online 25 July 2020

of most interest, the vessel must be cut longitudinally and mounted *en face*. Thus, imaging is most commonly performed on straight vessel segments without large branches; mounting more complex geometries flat is challenging. Additionally, whilst the current technique enables albumin uptake to be resolved in 3D, the necessary tissue manipulation results in a loss of spatial information, making point-by-point comparisons with other markers, such as computed wall shear stress (WSS), unreliable. A non-destructive method where the vessel can be imaged intact in a truly 3D fashion would have great utility.

Here we present such a method based on a combination of optical clearing and confocal microscopy. The heterogeneous composition of uncleared tissue causes light to scatter and refract at different angles, leading to signal attenuation. Transmittance can be increased by treating the tissue with optical clearing agents (OCAs), thus replacing the water and lipid, which have a low refractive index (RI), with a medium whose RI more closely matches that of the other components [7]. Clearing agents are classed in three categories: solvent-based, aqueous and hydrogel embedding. The former involves dehydrating and equilibrating the tissue in organic solvents (e.g. benzyl alcohol:benzyl benzoate (BABB)) [6,8,9]. Aqueous methods involve immersing the tissue in solutions of sugars such as fructose (SeeDB [10]) or sucrose (CUBIC [11]). Hydrogel embedding causes tissue transparency by replacing lipids with acrylamide/bisacrylamide (CLARITY [12]). These methods have revolutionised the use of microscopy in embryology and brain studies [6,13].

All OCAs have their advantages and pitfalls. For example, clearing tissue with aqueous-based or hydrogel embedding methods can take days or weeks, limiting the procedure to small samples [10,11,14,15]. However, the tissue architecture is preserved, unlike with solvent-based techniques, where some tissue shrinkage has been reported [16]. Despite this, the use of organic solvents such as BABB provides excellent tissue transparency in a wide range of tissues and is both rapid (minutes) and inexpensive [14,17].

In the present work, BABB was employed to overcome the inherently poor penetration of light into arterial tissue, enabling confocal imaging of intact vessels; light was able to penetrate the rat brachiocephalic artery (BCA; diameter approx. 1 mm) from the adventitia on one side, through to the adventitia on the other, and to image the aorto-BCA junction, giving nearly distortion-free 3D reconstruction of the BCA and tracer fluorescence within it. It was also found to be compatible with immunofluorescence staining and with imaging of experimental atherosclerosis despite the removal of lipid.

2. Materials and methods

Methods for the main permeability experiments are given here. Methods for the illustrative results concerning immunostaining and lesion detection are given in the Supplementary Materials.

2.1. Animals

All animal experiments complied with the Animals (Scientific Procedures) Act 1986 and were approved by the Local Ethical Review Process Committee of Imperial College London (Home Office Licence Licences PPL 70/733 and PPL P15180DF2). Healthy male Sprague-Dawley rats (Charles River Laboratories, UK) weighing between 230 and 290 g (n = 15) were housed in groups of 5 at 18–22 °C on a 12 h light:dark cycle and fed a standard laboratory diet with tap water *ad libitum*.

2.2. In vivo protocol

Rats were anaesthetised (induction: 5% isoflurane, maintenance: 1.5–2.5% isoflurance) and rhodamine-albumin tracer (150 mg/kg, prepared as described in Ref. [1]) was administered via the lateral tail vein (n = 10); in control experiments the tracer was omitted (n = 5). After 30 min, sodium pentobarbital (Euthatal, approx. 140 mg/kg iv) was administered and, after a midline thoracotomy, the left ventricle was cannulated. The dose of Euthatal was chosen to keep the heart beating, and hence to avoid complete depressurisation. The arterial system was flushed with 30 ml of heparinised saline (200 U/ml heparin, 0.9% NaCl) followed by 30 min of *in situ* fixation with 15% formaldehyde (VWR chemicals), both at physiological pressure. A small incision in the right atrium permitted drainage of the perfusate. The aortic arch and its daughter vessels were excised and stored overnight in 15% formaldehyde.

2.3. Tissue preparation

The tissue was washed in PBS and dehydrated in a graded series of ethanol (70, 90 and 100%) for 5 min each. BABB was prepared by combining benzyl alcohol with benzyl benzoate (2:1 v/v). The aorta was placed in a 1:1 v/v mixture of ethanol and BABB for approximately 5 min until the vessel sunk to the bottom of the vial, and then transferred to 100% BABB. Specimens, which became translucent within minutes, were stored in BABB.

2.4. Confocal microscopy

The optically-cleared aortic arch with its daughter vessels was placed horizontally on a glass coverslip and submerged in a drop of BABB. Imaging was performed with an inverted Leica TCS SP5 laser scanning confocal microscope with a computer-controlled motorised stage and 10 × 0.3NA dry lens. Tissue autofluorescence and rhodamine-albumin were excited at 458 nm and 561 nm and detected at 465–515 nm and 595–610 nm, respectively. The voxel size was 1.2 × 1.2 × 1.5 μm in the *x*-, *y*- and *z*-directions, respectively. The photomultiplier (PMT) gain setting was adjusted for each vessel to ensure that the maximum pixel intensity was just below saturation. To reduce in-plane non-uniformity of signal intensity due to the geometry of the optics, a zoom setting of 1.2 was used. Two overlapping volumes of interest (VOI) termed “upper” and “lower” were imaged (see Fig. 1A); data were acquired slice-by-slice in the *z*-direction in each VOI. Fig. 1B and C shows example optical sections and Fig. 1D shows volume renderings from one dataset. Data are presented in arbitrary units (A.U.) of signal intensity. The length of BCA imaged was 2.1 ± 0.66 mm (mean ± SEM) and scanning took approximately 45 min.

For one rat, acquisition was extended to four VOIs, including segments of the aortic arch, to assess the use of the technique for imaging larger structures.

2.5. Image processing pipeline

2.5.1. Finding the luminal surface

3D image volumes were resampled to give an isotropic voxel size of 1.5 μm and median filtered (kernel size 3) to reduce noise using Visualisation Toolkit (VTK)-Python scripts (www.vtk.org [18]). Level set segmentation in the Vascular Modelling Toolkit (VMTK) (www.vmtk.org [18,19]) was used to find the luminal surface in the autofluorescence image volumes. This segmentation generates a surface conforming to the regions with greatest intensity gradients. Level sets were initialised using the fast marching method as follows. Source and target seeds were selected in the image volume at each end of the vessel (Supplementary Fig. 1). An initial deformable model was created by propagating a front from each of the seeds until they met. A threshold value approximately equal to the mean intensity of the lumen was chosen to ensure the wave propagation did not extend beyond the artery wall. The deformable model was then refined through 500 iterations to produce the final level set. The marching cubes algorithm was used to generate a surface mesh from the deformable model.

Performing the level set segmentation on the original image volume

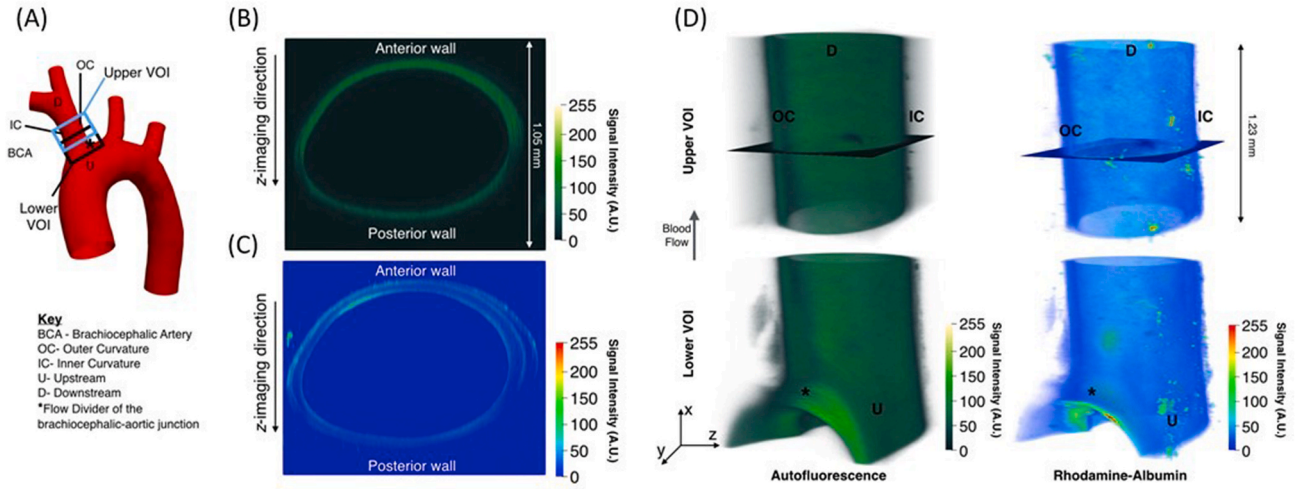

Fig. 1. Position of the VOIs with respect to the whole aortic arch (A). A cross-section of the BCA for the autofluorescence (B) and rhodamine-albumin (C) channels in arbitrary units (A.U.) of signal intensity. Volume renderings of each VOI for autofluorescence and rhodamine-albumin data (D). Mean blood flow direction is from upstream (U) to downstream (D).

(1.5 μm voxel size) was time consuming (> 8 h) and produced a 'coarse' surface compared to the mesh generated using a down-sampled image volume (10.2 μm); the mesh generated from the low resolution dataset was smoother and represented the lumen more appropriately (Supplementary Fig. 2), whilst the time required to segment the image volume was drastically reduced, to 10 min. Therefore, the autofluorescence channel was routinely down-sampled to 10.2 μm before segmentation.

2.5.2. Calculating the tracer sum

The low-resolution surface was used to probe the rhodamine-albumin image volume with isotropic 1.5 μm voxel size, using a purpose-written VTK-Python script. At every mesh vertex, normals were projected from the surface into the wall to a distance of 10 μm (Supplementary Fig. 3A). The signal intensity of the image volume was determined at 1 μm intervals along these normals and summed, and this tracer uptake was then mapped onto the surface. Since each BCA was acquired at a unique PMT gain setting, the signal intensity for each map was adjusted using a signal intensity-PMT gain calibration curve (see Supplementary Materials).

2.5.3. Stitching upper and lower segments together

Upper and lower segments of the BCA were aligned by landmark-based rigid registration using the Image Registration Toolkit (IRTK) (https://biomedia.doc.ic.ac.uk/software/irtk/, Licence from Ixico Ltd [20–23]). 7–10 landmarks were manually placed on each mesh in areas with matching features (Supplementary Fig. 3B). Meshes were then stitched in Blender (www.blender.org) using the available Boolean operation (union), which fused the two vessels together at their surface intersections. Internal overlapping faces were removed to produce the final surface. The mesh was subsequently smoothed using the Screened Poisson reconstruction method in Meshlab (http://www.meshlab.net [24,25]). The technique involves estimating an indicator function from the surface normals by calculating their divergence. The indicator function can then be used to re-compute the surface using the marching cubes algorithm. The surface resolution was approximately maintained.

2.5.4. Averaging branches

In order to show an average map of albumin uptake for all animals, it was necessary to project the data from each BCA surface on to a reference mesh. To achieve this, each branch (topologically a cylinder) was cylindrically mapped by the method presented in Ref. [26] (implemented in VMTK). Briefly, the vessel centerline was computed and every point on the mesh was assigned a longitudinal and circumferential coordinate (Supplementary Fig. 5). The circumferential coordinate system was always aligned to start at the outer curvature of the BCA. Using a purpose-written VTK-Python script, 2000 landmark points were automatically placed evenly around the circumference and along the length of the vessel. This procedure was repeated for all individual BCAs, one of which was arbitrarily termed the reference mesh. Subsequently, the landmark points were used to perform a non-rigid registration, using IRTK, between the vessel of interest and the reference mesh. This ensured the vessels matched the topology of the reference mesh more closely.

Using a VTK-Python script, rays were cast along the surface normals of the reference mesh. Rays were cast outwards from the subadjacent wall. Since vessels did not exactly deform to the topology of the reference mesh, it was also necessary to cast rays inwards (into the lumen) to ensure data from vessel segments found within the reference mesh were also included. To avoid rays intersecting the opposite wall, the ray length was limited to 500 μm. If an intersection between the ray and the surface was found, the data found at that coordinate point was projected onto the reference mesh. If no intersection was found, the value on the reference mesh was given a NaN value. Once the uptake for all BCAs was mapped onto the reference mesh, the average was computed.

For three datasets, cylindrically mapped BCAs were also virtually opened with a VTK-python script to visualise the uptake in 2D. Surface elements associated with circumferential coordinates at either side of a defined cutting line (-π to π) were removed. The vessel was subsequently 'unwrapped' to a plane.

2.6. Correcting image artefacts

2.6.1. Axial scaling (AS) correction

The surface mesh generated from the autofluorescence channel did not exactly represent the lumen in the rhodamine-albumin image volumes (Supplementary Fig. 8). RI mismatches between the coverglass, immersion medium and tissue cause axial (z) displacements in the position of the focal plane [25–29]. As a result of this phenomenon, not only did the BCA appear compressed in the axial dimension but there was also a noticeable difference in the position of the wall between the two image channels, attributed to the wavelength dependence of the RI. As this is a scaling effect, the phenomenon was more pronounced on the posterior wall. To compensate, an axial scaling (AS) factor of 1.004 was applied to the z-dimension of the surface mesh generated from the

autofluorescence channel before it was used to probe the rhodamine-albumin channel. The factor was determined experimentally, based on a method reported by Ref. [29] (see Supplementary Materials). Note that an absolute scaling correction was not performed, only an adjustment to make the geometry independent of wavelength.

2.6.2. Imaging the BCA en face

The 3D image data from three vessels were compared with data from the same optically-cleared vessels imaged *en face*. The aortic arch was removed so that the tissue would lie flat. The BCA was then cut open longitudinally and mounted endothelial surface down in BABB on a glass coverslip. To image the whole BCA, a tile-scan setting was used (with the same imaging parameters as for the intact tissue). Each tile consisted of a stack of slices in the *z*-direction, from the endothelium towards the adventitia. Subsequently, each *x*-*y* slice in the tile was divided by a 2D image of a uniformly fluorescent Chroma slide (imaged using the same parameters) for flatfield correction.

2.6.3. Statistics

The difference between experimental and contral data was assessed by Student's unpaired *t*-test. The difference in fluorescence intensity between pairs of regions was assessed using Student's paired *t*-test. The criterion for statistical significance was $p < 0.05$.

3. Results

3.1. Wall uptake of rhodamine-albumin mapped in intact vessels

The highest uptake of rhodamine-albumin occurred on the flow divider of the aorto-brachiocephalic junction and on the inner curvature of the BCA (Fig. 2A). Regions with highest standard error of the mean (SEM; Fig. 2B) coincided with regions of high albumin uptake; the magnitude of the SEM ranged from 1 to 20% of the mean values at the same location, indicating an overall low variability between rats. The average signal intensity for all branches was 340.69 ± 28.23 A U. Control experiments, with tracer omitted, produced a more uniform fluorescence with low average intensity (Fig. 2D) of 50.41 ± 7.26 A U. Tracer intensity was significantly higher than background ($p < 0.001$).

In the BCA of rats injected with tracer, fluorescence intensity was significantly higher in the inner curvature than the outer curvature, and in the upstream (proximal)) half than the downstream (distal) half. In control rats, not injected with tracer, there was no significant difference between the inner and outer curvatures, but there was a significant difference between the upstream and downstream halves (Table 1). The latter difference (~10% of the mean value) was proportionally much smaller than the equivalent difference in experimental values (~30% of the mean value) and presumably reflects a change in wall structure, and hence in autofluorescence, on progressing down the vessel. The ability to detect such small differences with a modest sample size illustrates the precision of the technique.

Table 1
Differences in fluorescence intensity between regions of the rat brachiocephalic artery.

	Inner curve	Outer curve	Upstream half	Downstream half
Experimental				
Mean (n = 10)	353.9	295.9	302.9	399.8
SEM	36.7	25.9	25.3	38.2
p value	0.014		< 0.001	
Control				
Mean (n = 5)	53.8	54.9	54.4	50.2
SEM	10.5	11.0	10.1	10.2
p value	0.413		0.007	

For the single rat in which the 3D method was extended to include segments of the aortic arch, elevated albumin uptake was additionally found on the outer curvature and proximal regions of the aortic arch (Fig. 3).

To validate the results obtained in intact vessels, albumin uptake in the walls three BCAs that had been imaged intact was compared to the equivalent data from the same vessels subsequently opened and imaged *en face*. The pattern of uptake was similar in all regions imaged by both methods except for an overall loss of signal intensity (but not a difference in local pattern) on the posterior wall of tissue imaged intact – i.e. the tissue that was furthest from the lens (Fig. 4).

The drop-off with depth was investigated further. Autofluorescence intensities were consistently higher in the anterior wall (closer to the lens) than the posterior wall (furthest from the lens) in all control datasets (e.g. Fig. 4B), even though the orientation of the specimen on the cover slip was randomised so that the anterior surface corresponded to different anatomical locations in different datasets. Fig. 4C shows the signal intensity against depth at one *x, y* location; assuming that there are no large scale variations in true autofluorescence intensity from one

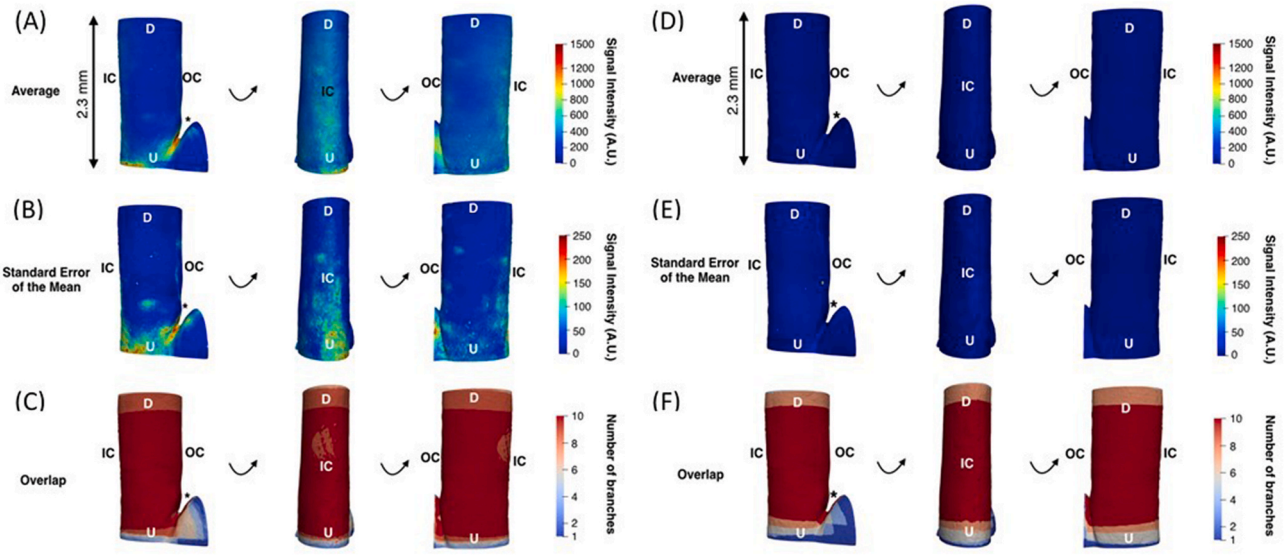

Fig. 2. Average uptake of rhodamine-albumin in the BCA (n = 10) (A). A uniform low background signal intensity was observed in control BCAs, where tracer was omitted (n = 5) (D). The SEM is in the same arbitrary units of signal intensity (note the different scale) for rhodamine-albumin (B) and controls (E). Overlap maps for rhodamine-albumin (C) and controls (F) show the number of branches accounting for the average at each location. Mean BCA blood flow is from bottom to top.

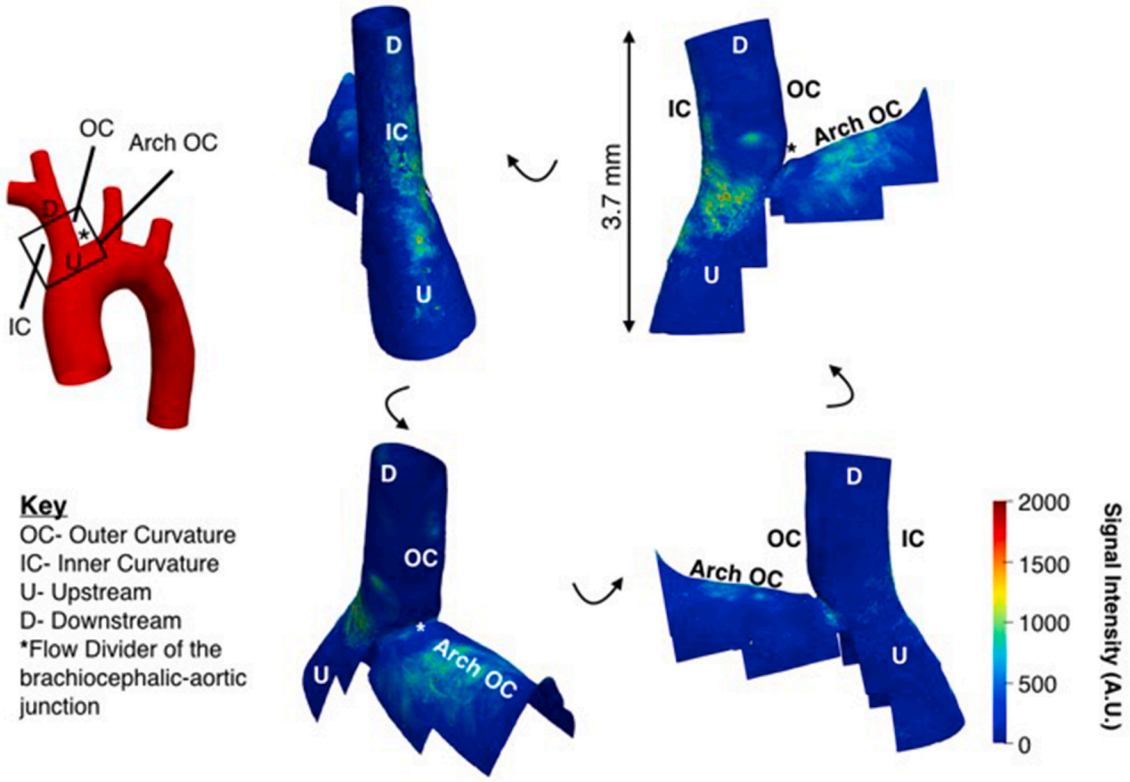

Fig. 3. For one dataset, imaging uptake of rhodamine-albumin was extended to regions of aorta further upstream and downstream of the BCA.

side of the vessel to the other (see Table 1, Controls, inner vs outer curvature), then approximately 30% of the signal intensity was lost from the anterior to posterior wall. Since the depthwise slices were acquired sequentially, the role photobleaching was investigated, as described in the Supplementary Materials; photobleaching appeared too slow to be a plausible cause of the bias.

3.2. Optical clearing was compatible with immunostaining

An *en face* image of PECAM-1 (CD31) immunostaining in rabbit descending thoracic aorta that has been fixed between antibody treatment and optical clearing is shown in Fig. 5A. It is evident that labelling of inter-endothelial junctions was preserved.

3.3. Optical clearing was compatible with lesion detection

Example images are of tissue from a male *apoE*$^{-/-}$ mouse fed a fat-rich diet for 25 weeks from weaning. An *en face* image of the whole outer curvature of the aortic arch, including branch mouths and lesions stained with Oil Red O, is shown in Fig. 5B. It was obtained by conventional epifluorescence microscopy prior to optical clearing. The classical pattern of the lesions filling, or nearly filling, the branch ostia is evident.

Tissue autofluorescence around the origin of the left subclavian artery, imaged after optical clearing, is shown in Fig. 5C–E. (The Oil Red O staining was removed by BABB.) Renderings of the 3-D data set show the geometry of the branch, and the orientation of the two orthogonal planes through the branch that were examined by extracting 2-D data from the full image. The normal wall and lesions are clearly distinguishable in the 2-D planes by their different structures and from the voids in the lesion areas where lipid was extracted during optical clearing.

4. Discussion

The rat BCA and aorto-brachiocephalic junction were imaged intact and uptake of circulating albumin by the vessel wall was mapped with micron-scale spatial resolution in a truly 3D fashion for the first time. Despite a vessel diameter of approximately 1 mm, fluorescence was still detectable by confocal microscopy on the posterior wall of the intact BCA; this was made possible by homogenisation of RIs using the BABB optical clearing technique. This penetration distance is approximately an order of magnitude greater than the depth in uncleared tissue that can be imaged *en face* with the same microscope. (Although the greater part of the 1 mm was arterial lumen in the present case, similar increases in penetration depth are also seen when that is not the case – see Supplementary Fig. 10). The method was also shown to be capable of imaging larger structures: the technique was extended to regions of the aortic arch as well as the BCA. Signal intensity in the experimental group was many times higher than in the control (i.e. no tracer) group, where a low and more uniform fluorescence was observed. There was good agreement between the new technique and the pattern of uptake obtained when imaging the same vessels *en face*. It is likely that increased depth penetration could also be achieved by two-photon microscopy or light-sheet microscopy in conjunction with optical clearing. However, the present method uses equipment that is more widely available.

Uptake of albumin was highest in the flow divider of the aorto-brachiocephalic junction, and in the initial segment and inner curvature of the BCA. The relatively low magnitude of the SEM at each point in the map suggested low variability between rats. To our knowledge, there have been no previous studies mapping the pattern of macromolecule uptake in the rat BCA. However, Phinikaridou et al. [30] detected elevated uptake of labelled-albumin in the inner wall of the BCA of *apoE*$^{-/-}$ mice fed a high-fat diet, using an MRI-based method, and our own group (Mohri Z. et al., unpublished data, 2015) observed elevated uptake of rhodamine-albumin around branch mouths of

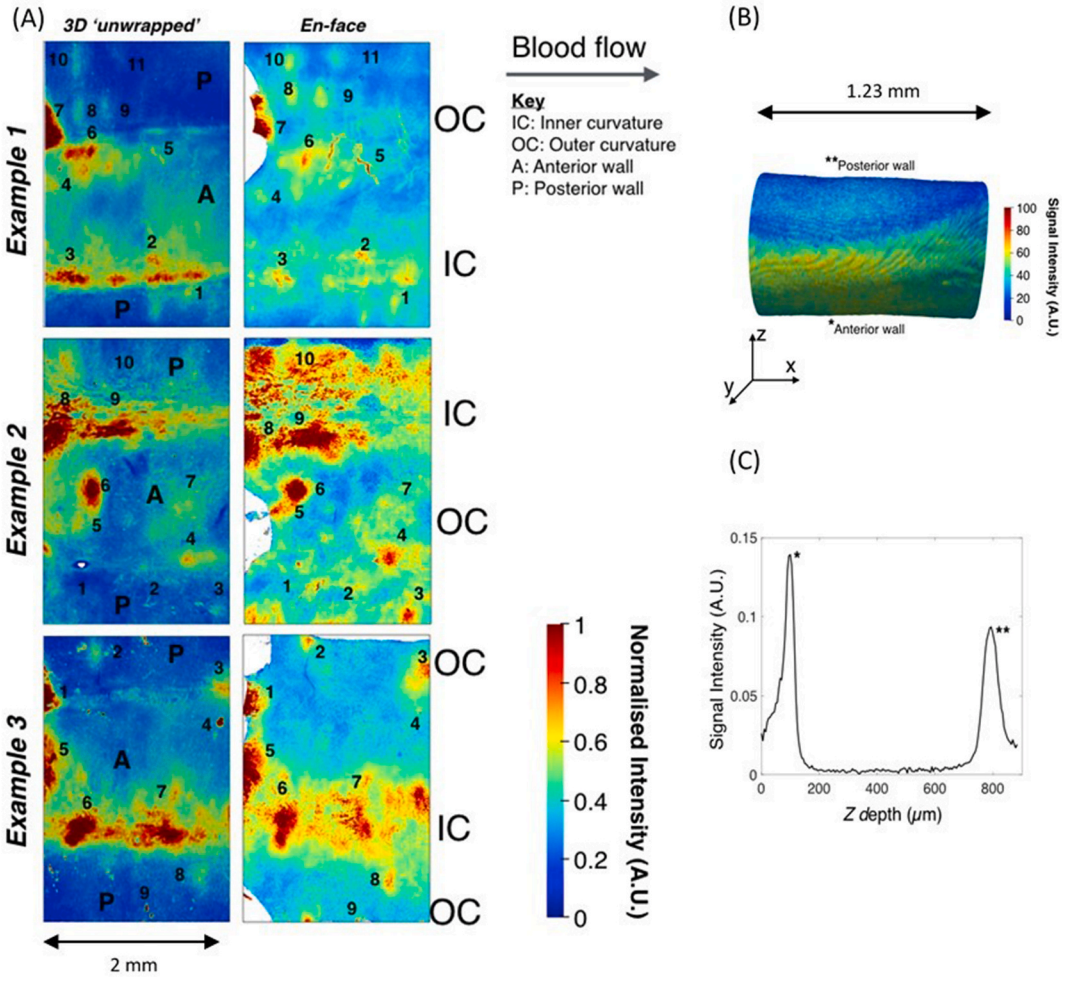

Fig. 4. (A) For datasets from three vessels, the intact BCAs were virtually 'unwrapped' along the sagittal plane. The real vessels were physically cut open at the same position and imaged en face. Data were normalised to the 98th intensity percentile in each image. Salient features in the patterns are numbered for comparison between the techniques: OC and IC indicate the outer and inner curvature of the BCA, respectively. "A" represents the anterior wall (i.e. nearest the lens when imaged intact) and "P" the posterior wall (furthest from the lens). Mean blood flow is from left to right. White areas represent areas where imaging failed due to the tissue not flattening perfectly. (B) Signal loss with depth from the anterior to the posterior wall for one control dataset. (C) Signal intensity against depth for one x, y location.

vessels in the aortic arch of *apoE*$^{-/-}$ mice in a study using confocal microscopy of *en face* preparations.

Disease patterns have been examined in the BCA of various species, although not in rats, which are not prone to experimental atherosclerosis. McGill et al. [31] found lesions around the origin of the BCA in dogs fed a high-fat diet for 8 weeks and many studies have identified the presence of highly eccentric plaques in the BCA of *apoE*$^{-/-}$ mice [32–37]. Atherosclerotic lesion frequencies have been studied at the bifurcation of the human BCA, where the pattern is again nonuniform [38,39]. Thus although the disease clearly has a patchy distribution in this vessel, we are not aware of any studies that can be directly compared with the distribution of tracer described above.

The pattern of albumin uptake, and of disease, might depend on local haemodynamic influences, particularly WSS. The current consensus is that areas experiencing low and oscillatory WSS are most prone to atherosclerosis [40], although this has been questioned [41]. The BCA is curved, at least in its proximal part. In a planar curved vessel, it is expected that the velocity profile becomes skewed by secondary motions so that the outer wall experiences high WSS and the inner wall experiences low WSS. This difference is exaggerated if there is flow separation on the inner wall. A number of computational simulations of flow in the mouse aortic arch and at least the proximal BCA appear to support this distribution of WSS for anatomically-realistic geometries [42–45]. If that also applies to the rat BCA, then the elevated albumin uptake on the inner curvature correlates with low WSS.

The situation at the flow divider is more complex. In general, high WSS is expected on both sides of it, since a new boundary layer has to develop. On the other hand, there should also be a stagnation point, where fluid is stationary and WSS reduces to zero, on the tip of the flow divider or close to it. The precise location may vary during the cardiac cycle, leading to a larger region of low average WSS. Consistent with these expectations, CFD studies of WSS in the mouse aortic arch do generally show high WSS on the flow divider, and in some cases the resolution and/or geometric accuracy permit low WSS on at least part of the tip to be visualised [42–44]. Computational modelling of flow in the rat and a precise comparison would be required to determine whether the elevated uptake we observed at the flow divider correlates better with the low or high WSS regions, or indeed with other features of the flow. The data processing techniques described above provide a 3-D surface representation of uptake that would readily allow such a comparison. (For simpler cases, less complex processing would suffice; even extracting simple cross sections through the vessel would give valuable data on variation in tracer uptake.)

The 3D imaging technique reported here may have some limitations. It is possible that the method for summing tracer uptake could have been a source of error. Normals with of length of 10 μm were projected from the luminal surface into the wall and the voxel intensity

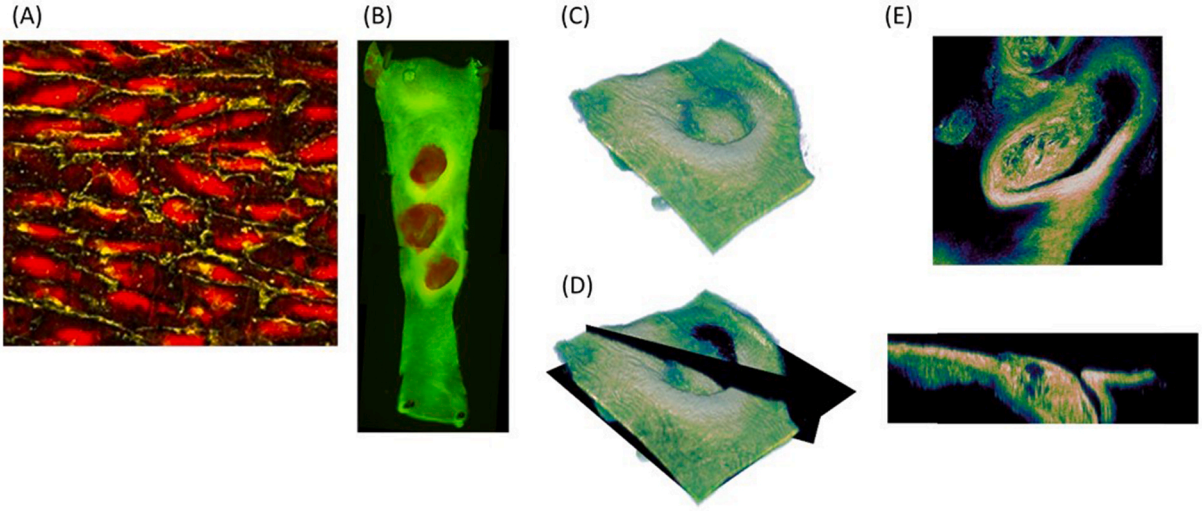

Fig. 5. (A) En face confocal image of an aorta that was stained with monoclonal mouse anti-human CD31 and Alexa Fluor 488-labelled goat anti-mouse IgG (yellow) and Qnuclear nuclear stain (red), then post-fixed and optically cleared. The image has dimension of 133 × 116 μm (x, y). (B) The outer curvature of the aortic arch, with the root at the top of the image, viewed en face. The three branch ostia are the origins of, from top to bottom, the brachiocephalic, left common carotid and subclavian arteries. The image was acquired by conventional epifluorescence microscopy (4× objective and standard Zeiss filter sets for fluorescein and rhodamine) before optical clearing and hence shows the red fluorescence from lipid stained with Oil Red O, as well as green autofluorescence. Slight discontinuities in the geometry arise from inaccuracies in tile stitching. (C) 3-D rendering of autofluorescence from the aortic region (area approximately 1.2 × 1.2 mm) around the mouth of the left subclavian artery and the initial portion of the branch itself. The segment was optically cleared before imaging. (D) The same rendering but with two 2-D image planes indicated as black surfaces. (E) The 2-D images, approximately parallel to and just outside the aortic wall (Top) and perpendicular to the aortic wall, longitudinally through the centre of the branch (Bottom). The normal wall and the occlusive lesion on the upstream lip of the branch are clearly distinguishable from the structure revealed by autofluorescence, and from the voids in the lesion where lipid was extracted during optical clearing. The severely stenosed lumen of the subclavian is visible as a narrow dark area between the surface of the lesion and the flow divider. (For interpretation of the references to colour in this figure legend, the reader is referred to the Web version of this article.)

in the rhodamine-albumin channel was detected at 1 μm intervals along the normals. As the surface was non-planar, it is possible that some voxels may have been included twice and some regions may have been undersampled. Errors of this type would have been most severe in areas of high local curvature.

A second source of error is apparent from the observation that signal intensity in the wall furthest from the lens was consistently lower than in the wall nearest the lens; that was true for autofluorescence, even though the orientation of the vessel was randomised and autofluorescence is expected to be relatively uniform. Signal drop-off with depth is dramatically reduced by optical clearing; without the use of BABB, it would have been much greater (see Supplementary Materials). Nevertheless, some drop-off appears to remain. A number of methods exist for correcting such errors; they involve estimating or computing an attenuation function experimentally, with a ray tracing geometrical approach [46,47] or with statistical methods [48,49]. In the present study, however, we used the simpler method of positioning vessels randomly on the microscope slide, so that there would have been no systematic bias in which wall was nearer to or further from the lens, minimising effects of drop-off in the average data and obviating the need for correction.

A final source of error that we investigated was the effect of photobleaching. The confocal optics are such that out-of-focus regions of the tissue remain illuminated as each slice is acquired [50]. To measure the effect of this, a vessel that had taken up rhodamine-albumin was repeatedly scanned. By the 4th repeat, the signal intensity had reduced by 10%. Tissue pretreated with an anti-fade agent for 24 h showed negligible signal loss (see Supplementary Materials). Whilst photobleaching was not thought to be a major source of error in the present study, the treatment of tissue with an anti-fade agent before imaging is desirable and should be incorporated in the methodology.

The major focus of the present study was the investigation of tracer uptake by the arterial wall. Nevertheless, we also examined the compatibility of solvent-based optical clearing with detection of immunostaining and of lipid-rich arterial lesions. Our experience is that conventional antibody staining does not survive optical clearing. Modified aqueous clearing methods do permit immunostaining (e.g. [51]) but here we used the simpler method of secondary fixation following immunostaining, to immobilise the antibodies during subsequent clearing with BABB. Immunostaining of PECAM-1 at endothelial cell borders was visible using this technique. We also found that atherosclerotic lesions could be identified from characteristic structural changes in the wall, even though the lipid (and lipid staining) is extracted during clearing with BABB. A similar method has been used in optical tomographic imaging of the mouse aorta [52].

In conclusion, wall uptake of albumin was mapped in a truly 3D fashion in an intact artery for the first time. The conserved geometry of the vessel allows for more accurate spatial correlations between permeability, disease and haemodynamic influences, particularly in regions where vessel geometries are complex, and hence will further our understanding of the pathogenesis of atherosclerosis.

Financial support

We thank the EPSRC Centre for Doctoral Training in Medical Imaging and the BHF for funding this work.

CRediT authorship contribution statement

Marta Dazzi: Formal analysis, Writing - original draft. **Ethan M. Rowland:** Formal analysis. **Zahra Mohri:** Formal analysis. **Peter D. Weinberg:** Conceptualization, Writing - original draft.

Declaration of competing interest

Conflict of Interest Statement: All authors declare that they have no actual or potential conflict of interest including financial, personal or other relationships with other people or organizations within three

years of beginning the submitted work that could inappropriately influence, or be perceived to influence, the work.

Appendix A. Supplementary data

Supplementary data to this article can be found online at https://doi.org/10.1016/j.atherosclerosis.2020.07.002.

References

[1] L.A. Clarke, Z. Mohri, P.D. Weinberg, High throughput en face mapping of arterial permeability using tile scanning confocal microscopy, Atherosclerosis 224 (2012) 417–425, https://doi.org/10.1016/j.atherosclerosis.2012.08.001.

[2] E.L. Bailey, E. Bazigou, P.S. Sowinski, P.D. Weinberg, Mass transport properties of the rabbit aortic wall, PLoS One 10 (2015) e0120363, , https://doi.org/10.1371/journal.pone.0120363.

[3] L. Huang, K.L. Chambliss, X. Gao, I.S. Yuhanna, E. Behling-Kelly, S. Bergaya, M. Ahmed, P. Michaely, K. Luby-Phelps, A. Darehshouri, L. Xu, E.A. Fisher, W.P. Ge, C. Mineo, P.W. Shaul, SR-B1 drives endothelial cell LDL transcytosis via DOCK4 to promote atherosclerosis, Nature 569 (2019) 565–569, https://doi.org/10.1038/s41586-019-1140-4.

[4] J.R. Kraehling, J.H. Chidlow, C. Rajagopal, M.G. Sugiyama, J.W. Fowler, M.Y. Lee, X. Zhang, C.M. Ramírez, E.J. Park, B. Tao, K. Chen, L. Kuruvilla, B. Larriveé, E. Folta-Stogniew, R. Ola, N. Rotllan, W. Zhou, M.W. Nagle, J. Herz, K.J. Williams, A. Eichmann, W.L. Lee, C. Fernández-Hernando, W.C. Sessa, Genome-wide RNAi screen reveals ALK1 mediates LDL uptake and transcytosis in endothelial cells, Nat. Commun. 7 (2016), https://doi.org/10.1038/ncomms13516.

[5] M. Gouverneur, B. Berg, M. Nieuwdorp, E. Stroes, H. Vink, Vasculoprotective properties of the endothelial glycocalyx: effects of fluid shear stress, J. Intern. Med. 259 (2006) 393–400, https://doi.org/10.1111/j.1365-2796.2006.01625.x.

[6] D.S. Richardson, J.W. Lichtman, Clarifying tissue clearing, Cell 162 (2015) 246–257, https://doi.org/10.1016/j.cell.2015.06.067.Clarifying.

[7] C.P. Neu, T. Novak, K.F. Gilliland, P. Marshall, S. Calve, Optical clearing in collagen- and proteoglycan-rich osteochondral tissues, Osteoarthritis Cartilage 23 (2015) 405–413, https://doi.org/10.1016/j.joca.2014.11.021.

[8] A. Ertürk, C.P. Mauch, F. Hellal, F. Förstner, T. Keck, K. Becker, N. Jährling, H. Steffens, M. Richter, M. Hübener, E. Kramer, F. Kirchhoff, H.U. Dodt, F. Bradke, Three-dimensional imaging of the unsectioned adult spinal cord to assess axon regeneration and glial responses after injury, Nat. Med. 18 (2011) 166–171, https://doi.org/10.1038/nm.2600.

[9] S. Ivins, C. Roberts, B. Vernay, P.J. Scambler, Analysis of coronary vessels in cleared embryonic hearts, JoVE 118 (2016) e54800, , https://doi.org/10.3791/54800.

[10] M.T. Ke, S. Fujimoto, T. Imai, SeeDB, A simple and morphology-preserving optical clearing agent for neuronal circuit reconstruction, Nat. Neurosci. 16 (2013) 1154–1161, https://doi.org/10.1038/nn.3447.

[11] E.A. Susaki, K. Tainaka, D. Perrin, F. Kishino, T. Tawara, T.M. Watanabe, C. Yokoyama, H. Onoe, M. Eguchi, S. Yamaguchi, T. Abe, H. Kiyonari, Y. Shimizu, A. Miyawaki, H. Yokota, H.R. Ueda, Whole-brain imaging with single-cell resolution using chemical cocktails and computational analysis, Cell 157 (2014) 726–739, https://doi.org/10.1016/j.cell.2014.03.042.

[12] K. Chung, J. Wallace, S.Y. Kim, S. Kalyanasundaram, A.S. Andalman, T.J. Davidson, J.J. Mirzabekov, K.A. Zalocusky, J. Mattis, A.K. Denisin, S. Pak, H. Bernstein, C. Ramakrishnan, L. Grosenick, V. Gradinaru, K. Deisseroth, Structural and molecular interrogation of intact biological systems, Nature 497 (2013) 332–337, https://doi.org/10.1038/nature12107.

[13] A. Azaripour, T. Lagerweij, C. Scharfbillig, A.E. Jadczak, B. Willershausen, C.J. Van Noorden, A survey of clearing techniques for 3D imaging of tissues with special reference to connective tissue, Prog. Histochem. Cytochem. 51 (2016) 9–23, https://doi.org/10.1016/j.proghi.2016.04.001.

[14] H. Hama, H. Kurokawa, H. Kawano, R. Ando, T. Shimogori, H. Noda, K. Fukami, A. Sakaue-Sawano, A. Miyawaki, Scale: a chemical approach for fluorescence imaging and reconstruction of transparent mouse brain, Nat. Neurosci. 14 (2011) 1481–1488, https://doi.org/10.1038/nn.2928.

[15] H. Kolesová, M. Čapek, B. Radochová, J. Janáček, D. Sedmera, Comparison of different tissue clearing methods and 3D imaging techniques for visualization of GFP-expressing mouse embryos and embryonic hearts, Histochem. Cell Biol. 146 (2016) 141–152, https://doi.org/10.1007/s00418-016-1441-8.

[16] H.U. Dodt, U. Leischner, A. Schierloh, N. Jährling, C.P. Mauch, K. Deininger, J.M. Deussing, M. Eder, W. Zieglgänsberger, K. Becker, Ultramicroscopy: three-dimensional visualization of neuronal networks in the whole mouse brain, Nat. Methods 4 (2007) 331–336, https://doi.org/10.1038/nmeth1036.

[17] P.J. Keller, H.U. Dodt, Light sheet microscopy of living or cleared specimens, Curr. Opin. Neurobiol. 22 (2012) 138–143, https://doi.org/10.1016/J.CONB.2011.08.003.

[18] W. Schroeder, K. Martin, B. Lorensen, The Visualization Toolkit, fourth ed., (2006) Kitware.

[19] L. Antiga, M. Piccinelli, L. Botti, B. Ene-Iordache, A. Remuzzi, D.A. Steinman, An image-based modeling framework for patient-specific computational hemodynamics, Med. Biol. Eng. Comput. 46 (2008) 1097–1112, https://doi.org/10.1007/s11517-008-0420-1.

[20] D. Rueckert, C. Hayes, C. Studholme, P. Summers, M. Leach, D.J. Hawkes, Non-rigid registration of breast MR images using mutual information, IEEE Trans. Med. Imag. 18 (1999) 712–721.

[21] C. Studholme, D.L.G. Hill, D.J. Hawkes, An overlap invariant entropy measure of 3D medical image alignment, Pattern Recogn. 32 (1999) 71–86, https://doi.org/10.1016/S0031-3203(98)00091-0.

[22] E.R. Denton, L.I. Sonoda, D. Rueckert, S.C. Rankin, C. Hayes, M.O. Leach, D.L. Hill, D.J. Hawkes, Comparison and evaluation of rigid, affine, and nonrigid registration of breast MR images, J. Comput. Assist. Tomogr. 23 (1999) 800–5 http://www.ncbi.nlm.nih.gov/pubmed/10524870 accessed January 24, 2019.

[23] J.A. Schnabel, D. Rueckert, M. Quist, J.M. Blackall, A.D. Castellano-Smith, T. Hartkens, G.P. Penney, W.A. Hall, H. Liu, C. Truwit, F.A. Gerritsen, D.L.G. Hill, D.J. Hawkes, A generic framework for non-rigid registration based on non-uniform multi-level free-form deformations, in: W.J. Niessen, M.A. Viergever (Eds.), Med. Image Comput. Comput. Interv. - MICCAI 2001 - 4th Int. Conf. Proc. Springer-Verlag, 2001, pp. 573–581.

[24] P. Cignoni, M. Callieri, M. Corsini, M. Dellepiane, F. Ganovelli, G. Ranzuglia, MeshLab: an open-source mesh processing tool, Eurographics Ital. Chapter Conf. 2008, pp. 129–136, , https://doi.org/10.2312/LocalChapterEvents/ItalChap/ItalianChapConf2008/129-136.

[25] M. Kazhdan, H. Hoppe, Screened Poisson surface reconstruction, ACM Trans. Graph. 32 (2013) 1–13, https://doi.org/10.1145/2487228.2487237.

[26] L. Antiga, D.A. Steinman, Robust and objective decomposition and mapping of bifurcating vessels, IEEE Trans. Med. Imag. 23 (2004) 704–713, https://doi.org/10.1109/TMI.2004.826946.

[27] S. Hell, G. Reiner, C. Cremer, E.H.K. Stelzer, Aberrations in confocal fluorescence microscopy induced by mismatches in refractive index, J. Microsc. 169 (1993) 391–405, https://doi.org/10.1111/j.1365-2818.1993.tb03315.x.

[28] K.C. Neuman, E.A. Abbondanzieri, S.M. Block, Measurement of the effective focal shift in an optical trap Keir, Opt. Lett. 30 (2005) 1318–1320, https://doi.org/10.1016/j.dcn.2011.01.002 The.

[29] T.H. Besseling, J. Jose, A. Van Blaaderen, Methods to calibrate and scale axial distances in confocal microscopy as a function of refractive index, J. Microsc. 257 (2015) 142–150, https://doi.org/10.1111/jmi.12194.

[30] A. Phinikaridou, M.E. Andia, A. Protti, A. Indermuehle, A. Shah, A. Smith, A. Warley, M. Botnar, Noninvasive magnetic resonance imaging evaluation of endothelial permeability in murine atherosclerosis using an albumin-binding contrast agent, Circulation 126 (2012) 707–719, https://doi.org/10.1161/CIRCULATIONAHA.112.092098.

[31] H.C. McGill, J.C. Geer, R.L. Holman, Sites of vascular vulnerability in dogs demonstrated by Evans blue, Arch. Pathol. 64 (1957) 303–311 https://www.cabdirect.org/cabdirect/abstract/19581404054 accessed February 11, 2019.

[32] M.E. Rosenfeld, P. Polinsky, R. Virmani, K. Kauser, G. Rubanyi, S.M. Schwartz, Advanced atherosclerotic lesions in the innominate artery of the apoE knockout mouse, Arterioscler. Thromb. Vasc. Biol. 20 (2000) 2587–2592, https://doi.org/10.1161/01.ATV.20.12.2587.

[33] J.L. Johnson, C.L. Jackson, Atherosclerotic plaque rupture in the apolipoprotein E knockout mouse, Atherosclerosis 154 (2001) 399–406, https://doi.org/10.1016/S0021-9150(00)00515-3.

[34] C.L. Jackson, A.R. Bond, The fat-fed apolipoprotein e knockout mouse brachiocephalic artery in the study of atherosclerotic plaque rupture, J. Biomed. Biotechnol. 2011 (2011) 379069, , https://doi.org/10.1155/2011/379069.

[35] C. Parolini, M. Busnelli, G.S. Ganzetti, F. Dellera, S. Manzini, E. Scanziani, J.L. Johnson, C.R. Sirtori, G. Chiesa, Magnetic resonance imaging visualization of vulnerable atherosclerotic plaques at the brachiocephalic artery of apolipoprotein e knockout mice by the blood-pool contrast agent B22956/1, Mol. Imag. 13 (2014) 1–9, https://doi.org/10.2310/7290.2014.00012.

[36] A. Naumova, V. Yarnykh, M. Ferguson, M. Rosenfeld, C. Yuan, MR histology of advanced atherosclerotic lesions of ApoE- knockout mice, J. Phys. Conf. Ser. 677 (2016) 12008, , https://doi.org/10.1088/1742-6596/677/1/012008.

[37] D. Teupser, A.D. Persky, J.L. Breslow, Induction of atherosclerosis by low-fat, semisynthetic diets in LDL receptor-deficient C57BL/6J and FVB/NJ mice: comparison of lesions of the aortic root, brachiocephalic artery, and whole aorta (en face measurement), Arterioscler. Thromb. Vasc. Biol. 23 (2003) 1907–1913, https://doi.org/10.1161/01.ATV.0000090126.34881.B1.

[38] M. Kjaernes, A. Svindland, L. Walløe, S.O. Wille, Localization of early atherosclerotic lesions in an arterial bifurcation in humans, Acta Pathol. Microbiol. Scand. A. 89 (1981) 35–40 http://www.ncbi.nlm.nih.gov/pubmed/7013418 accessed February 11, 2019.

[39] M.E. DeBakey, G.M. Lawrie, D.H. Glaeser, Patterns of atherosclerosis and their surgical significance, Ann. Surg. 201 (1985) 115–132, https://doi.org/10.1097/00000658-198502000-00001.

[40] Y. Huo, X. Guo, G.S. Kassab, The flow field along the entire length of mouse aorta and primary branches, Ann. Biomed. Eng. 36 (2008) 685–699, https://doi.org/10.1007/s10439-008-9473-4.

[41] V. Peiffer, S.J. Sherwin, P.D. Weinberg, Does low and oscillatory wall shear stress correlate spatially with early atherosclerosis? A systematic review, Cardiovasc. Res. 99 (2013) 242–250, https://doi.org/10.1093/cvr/cvt044.

[42] J. Suo, D.E. Ferrara, D. Sorescu, R.E. Guldberg, W.R. Taylor, D.P. Giddens, Hemodynamic shear stresses in mouse aortas: implications for atherogenesis, Arterioscler. Thromb. Vasc. Biol. 27 (2007) 346–351, https://doi.org/10.1161/01.ATV.0000253492.45717.46.

[43] B. Trachet, A. Swillens, D. Van Loo, C. Casteleyn, A. De Paepe, B. Loeys, P. Segers, The influence of aortic dimensions on calculated wall shear stress in the mouse aortic arch, Comput. Methods Biomech. Biomed. Eng. 12 (2009) 491–499, https://doi.org/10.1080/10255840802695445.

[44] P. Assemat, K.K. Siu, J.A. Armitage, S.N. Hokke, A. Dart, J. Chin-Dusting, K. Hourigan, Haemodynamical stress in mouse aortic arch with atherosclerotic plaques: preliminary study of plaque progression, Comput. Struct. Biotechnol. J. 10

(2014) 98–106, https://doi.org/10.1016/j.csbj.2014.07.004.
[45] M.A. Van Doormaal, A. Kazakidi, M. Wylezinska, A. Hunt, J.L. Tremoleda, A. Protti, Y. Bohraus, W. Gsell, P.D. Weinberg, C.R. Ethier, Haemodynamics in the mouse aortic arch computed from MRI-derived velocities at the aortic root, J. R. Soc. Interface 9 (2012) 2834–2844, https://doi.org/10.1098/rsif.2012.0295.
[46] K. Rodenacker, S. Wuertz, S. Purkayastha, Depth intensity correction of biofilm volume data from confocal laser scanning microscopes, Image Anal. Stereol. 20 (2001) 556–560.
[47] D. Visser, F.C.A. Groen, G.J. Brakenhoff, Absorption and scattering correction in fluorescence confocal microscopy, J. Microsc. 163 (1991) 189–200.
[48] P.S.U. Adiga, B.B. Chaudhuri, Some efficient methods to correct confocal images for easy interpretation, Micron 32 (2001) 363–370.
[49] J.B.T.M. Roerdink, M. Bakker, An FFT-based method for attenuation correction in fluorescence confocal microscopy, J. Microsc. 169 (1993) 3–14.
[50] U. Bal, V. Andresen, B. Baggett, U. Utzinger, Intravital confocal and two-photon imaging of dual-color cells and extracellular matrix mimics, Microsc. Microanal. 19 (2013) 201–212, https://doi.org/10.1038/jid.2014.371.
[51] W. Li, R.N. Germain, M.Y. Gerner, Multiplex, quantitative cellular analysis in large tissue volumes with clearing-enhanced 3D microscopy (Ce3D), Proc. Natl. Acad. Sci. Unit. States Am. 114 (2017) E7321–E7330, https://doi.org/10.1073/pnas.1708981114.
[52] N.S. Kirkby, L. Low, J.R. Seckl, B.R. Walker, D.J. Webb, P.W. Hadoke, Quantitative 3-dimensional imaging of murine neointimal and atherosclerotic lesions by optical projection tomography, PLoS One 6 (2011) e16906, , https://doi.org/10.1371/journal.pone.0016906.